

Single-shot recognition of orbital angular momentum from speckles with spatially multiplexed point detection (SMPD)

Zhiyuan Wang,^{a,b,†} Haoran Li,^{c,d,†} Qi Zhao,^{c,d} Vinu R V,^{a,b} Xiaocong Yuan,^e Ziyang Chen,^{a,b,*} Puxiang Lai,^{c,d,f,*} and Jixiong Pu^{a,b}

^aHuaqiao University, College of Information Science and Engineering, Xiamen, 361021, China

^bHuaqiao University, Fujian Provincial Key Laboratory of Light Propagation and Transformation, Xiamen, 361021, China

^cHong Kong Polytechnic University, Department of Biomedical Engineering, Hong Kong, China

^dHong Kong Polytechnic University, Shenzhen Research Institute, Shenzhen, China

^eShenzhen University, Nanophotonics Research Center, Shenzhen Key Laboratory of Micro-scale Optical Information Technology, Institute of Microscale Optoelectronics, Shenzhen, 518060, China

^fHong Kong Polytechnic University, Photonics Research Institute, Hong Kong, China

Abstract. The widely adopted optical information detection strategies nowadays can be roughly classified into spatial-resolve-based and time-sequence-based methods. The former is highly reliant on detectors with spatial resolution that works in a limited spectrum range to capture the intensity distribution of the object, whereas the latter employs single-pixel detectors (SPDs) with improved reliability and stability in detection at the expense of time consumption due to sequential intensity recording. However, there is a scarcity of research on using high-performance SPDs for single-shot object information detection. To capture and extract features of objects efficiently and economically, in this work, we propose a single-shot optical information-detecting method, tentatively named spatially multiplexed point detection (SMPD) technology, in which some SPDs are randomly distributed at different locations to acquire the information of the object. To validate the validity of the proposed method, we demonstrate high-fidelity recognition of orbital angular momentum (OAM) modes from speckle patterns generated by the transmission of two orthogonally polarized vortex beams through a multimode fiber. It is feasible to apply this approach in wide applications, such as image transmission based on multiplexed-OAM decoding and recognizing hand-written digits. Compared with traditional image recognition methods, the new approach yields a recognition accuracy of over 98% with an effective detection area that is only 0.02% of its counterparts. With further engineering, the proposed method may spur many exciting developments in OAM-based optical communication systems, image classification, object detections, and other optical information detections.

Keywords: Orbital angular momentum, Single pixel detector, Multimode fiber, Deep learning, Speckle

*Address all correspondence to Ziyang Chen at ziyang@hqu.edu.cn and Puxiang Lai at puxiang.lai@polyu.edu.hk

[†]These authors contributed equally to this work.

1 Introduction

Detectors play a central role in most scenarios of imaging and object detection, such as target recognition, defect probing, and beam analysis. In a camera-based imaging system, a high-resolution sensor chip with many light-sensitive elements made by a silicon-based charge-coupled device (CCD) or complementary metal-oxide-semiconductor (CMOS) is usually involved to capture the object's spatial distribution^{1,2}. For sensing applications at wavebands like infrared and

deep ultraviolet, such silicon-based sensors are usually not suitable due to their small bandgap and weak absorption² and high-resolution sensor chips working in these wavebands are expensive or impractical¹⁻⁴. Furthermore, in scenarios accompanied with strong scattering and absorption losses, such as medical imaging⁶⁻⁸ and remote sensing^{9,10}, the weakly detected information is easily obscured in the background noise and the dark current of the multi-pixel detectors. In comparison, in a single-pixel detector (SPD)-based imaging system, one measures the light intensity with a single-pixel detector without spatial resolution, which brings advantages of wider sensing spectrum, cheaper price, higher detection sensitivity, lower dark counts, and faster response times^{1,2,11}. Although it secures a better measurement capability than multi-pixel cameras in situations with weak light intensities^{4,10,11}, the lack of spatial resolution and rigid requirement for object recognition or restoration have discouraged SPD from being employed in single-shot detections. Instead, demonstrated advancements in SPD-based technologies have primarily focused on unconventional imaging approaches like single-pixel imaging¹²⁻¹⁴ (SPI) and computational ghost imaging^{2,9} (CGI). These implementations are achieved through continuous time accumulation analysis of received intensity fluctuations, which undoubtedly requires additional equipment and time consumption.

In a regular imaging system, a point from the object is usually faithfully mapped to a specific point on the image plane, thus the object information can be extracted only by recording the entire spatial distribution of the image plane. This rule, however, sees exception when photons propagate within or through a highly scattering medium. The accumulated multiple scattering generates speckle patterns and seriously impairs the detection or interpretation of the imaging information¹⁵⁻²². Nevertheless, it projects many points from the object onto one point onto the image plane, and meanwhile one point from the object may have its projection at many points on the image plane.

Although complicated and seemingly random, the entire process actually can be described with a transmission matrix²³, which states that each region in the output field can be treated as the superposition of the entire incident light field due to the random transmission of light in the medium^{23,24}. Therefore, it is naturally inferred that a small portion of the speckle field can sufficiently represent the whole output field, and hence be utilized to reconstruct and recognize the information of the object. This presents unique and novel opportunities for imaging and sensing of a large field of view based on the detection of very few speckle grains.

One example of such scenario is the detection of OAM information of vortex beams, which has garnered attention in recent years due to its crucial role in many fields. Vortex beams²⁵⁻²⁹ have phase terms in the form of $\exp(il\theta)$, carrying OAM of $l\hbar$. Here, l is the topological charge and θ denotes the azimuthal angle. Since vortex beams with different numbers of OAM are mutually independent, the combination of various vortex beams can be used as information carriers^{28,30-32} in optical communications systems primarily based on technologies like OAM shift keying (OAM-SK) or OAM division multiplexing^{33,34}. Therefore, the recognition of OAM is extremely essential in these applications^{33,36-40}. Especially, when vortex beams propagate through a multimode fiber (MMF)^{38,41,42}, the most widely adopted light guide in optical communication, challenges occur in the detection scheme accompanying the generation of speckle patterns at the distal end of the MMF due to effects like mode coupling, superposition, and dispersion, among others^{22,38,41,42}. Traditional solutions based on interferometry or vortex diffraction grating⁴⁰ require a well-defined donut-shaped beam structure and hence are impractical for recognizing OAMs from speckle patterns. To overcome the challenge, approaches based on deep learning^{38,39,41}, transmission matrix⁴³, or Fourier spectra analysis of the cross-covariance function³⁷ have been proposed. Whilst effective,

these methods usually require a CCD or CMOS camera to capture the spatial intensity distribution of the speckle patterns.

Based on the unique “delocalization” feature of speckles as discussed above, one may recognize OAMs from a very small portion of the speckle field. In this work, we propose a novel approach, spatially multiplexed point detection (SMPD), to address the measurement challenges in OAM-based communication systems. This method exploits the delocalized characteristic for information encoding with a scattering medium, employing several SPDs to record optical intensities at sparse locations on the detection plane. Note that no spatial-resolved speckle patterns need to be recorded by a multi-pixel camera, nor time-sequential correlated intensities need to be recorded by a single SPD. By recording the intensities at several locations in the speckle field, SMPD retains a limited amount of spatial intensity information about the object. To demonstrate the feasibility of SMPD, we utilize the recognition of OAMs scrambled in speckle patterns generated by two orthogonally polarized vortex beams transmitted through an MMF as an example. To extract utmost information from limited intensity data, we design a neural network with two feature extract paths that analyze the input intensity sequence on different dimensions and concatenate the extracted features. With the aid of the neural network, the OAMs can be deciphered at high accuracy regardless of the limited spatial and intensity distribution information from measurements. Furthermore, we also show the feasibility of the proposed method in other applications, such as decoding multiplexed OAMs, recognizing the angle of axicon, and classifying handwritten digits.

2 Methodology

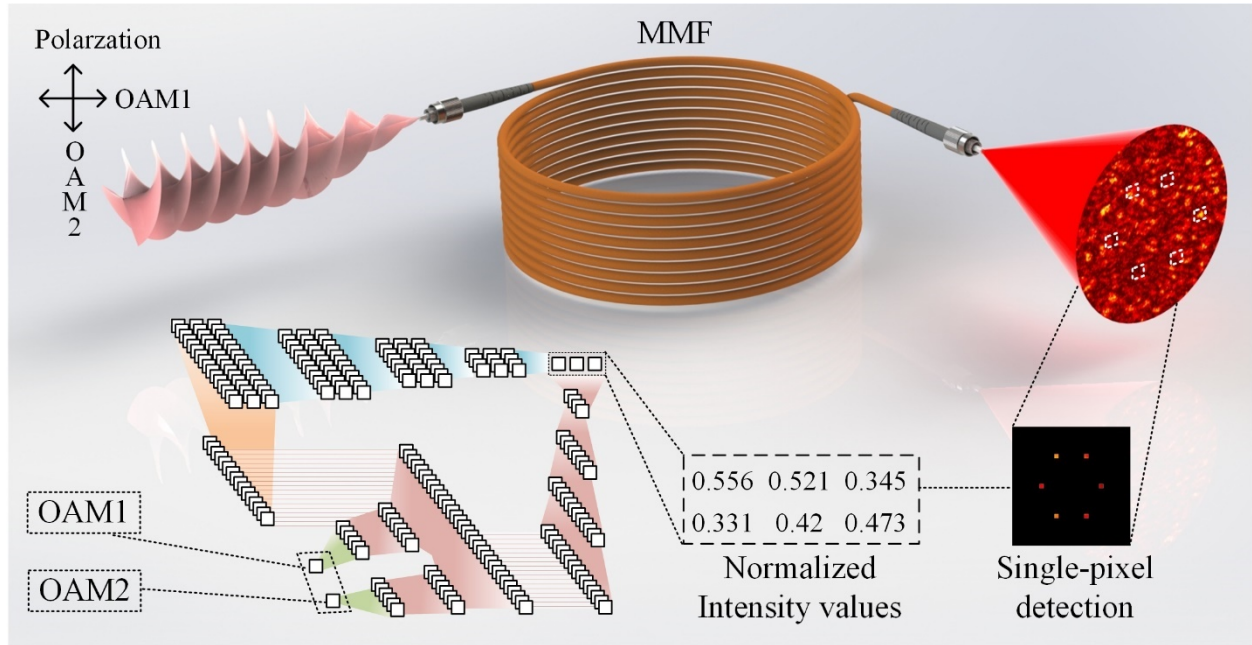


Fig. 1 Illustration of the proposed SMPD. The transmission of two orthogonally polarized vortex beams through an MMF generates a speckle field at the distal end of the MMF. The intensity values at several randomly selected locations in the speckle field are detected by a few SPDs and input into the designed neural network, which outputs/recognizes the OAMs of the input vortex beams.

The concept of SMPD is illustrated in Fig. 1, where the transmission of two orthogonally polarized vortex beams through an MMF generates a speckle pattern at the distal end of the fiber. Unlike conventional high-spatial-resolution or time-sequence detecting methods, SMPD utilizes single-shot detection based on several SPDs to simultaneously record the optical intensity values at sparse locations in the speckle field. The detections are input to a neural network termed as Recognizing OAM Artificial Neural Network (ROAM-ANN), which secures two paths to extract the features of the inputs in different dimensions and eventually outputs the encoded OAMs from the pointwise intensity sequences.

2.1 Experimental setup

In experiment, the intensity sequences are generated and collected by the setup shown in Fig. 2. A vertically polarized infrared laser output (Origami-10XP, 400 fs, 1 MHz, 1028 nm, Onefive) changes its polarization direction to 45° through transmitting a half-wave plate (HWP). The 45° polarized laser beam is divided into two paths of equivalent intensity but orthogonal polarizations by a polarizing beam splitter (PBS). Then, two spatial light modulators (SLM, X13138-03 and X13138-09, HAMAMATSU) are placed at the corresponding polarization direction and impose spiral phases onto the two horizontally and vertically polarized beams, respectively. The reflected and modulated vortex beams from the SLMs are recombined by the PBS and coupled into a MMF (diameter=62.5 μm , NA=0.275, length=20 meters, M31L20, Thorlabs) through an objective (O1, 10X, NA=0.25). Speckle fields are generated at the distal end of the MMF, which are converged by another objective (O2, 20X, NA=0.4) and finally captured by a CCD camera (Pike F421B, AVT). Note that instead of inputting the whole field of view of the speckle patterns to the neural network, in this study a mask is imposed onto the speckle patterns to sample several small regions to achieve spatially multiplexed point detection. Intensity values obtained from these point detectors are determined by calculating the total grayscale values within the designated area. In this sense, the CCD camera virtually serves as an array of SPDs, with each SPD accumulating the intensity values at the corresponding locations in the speckle pattern.

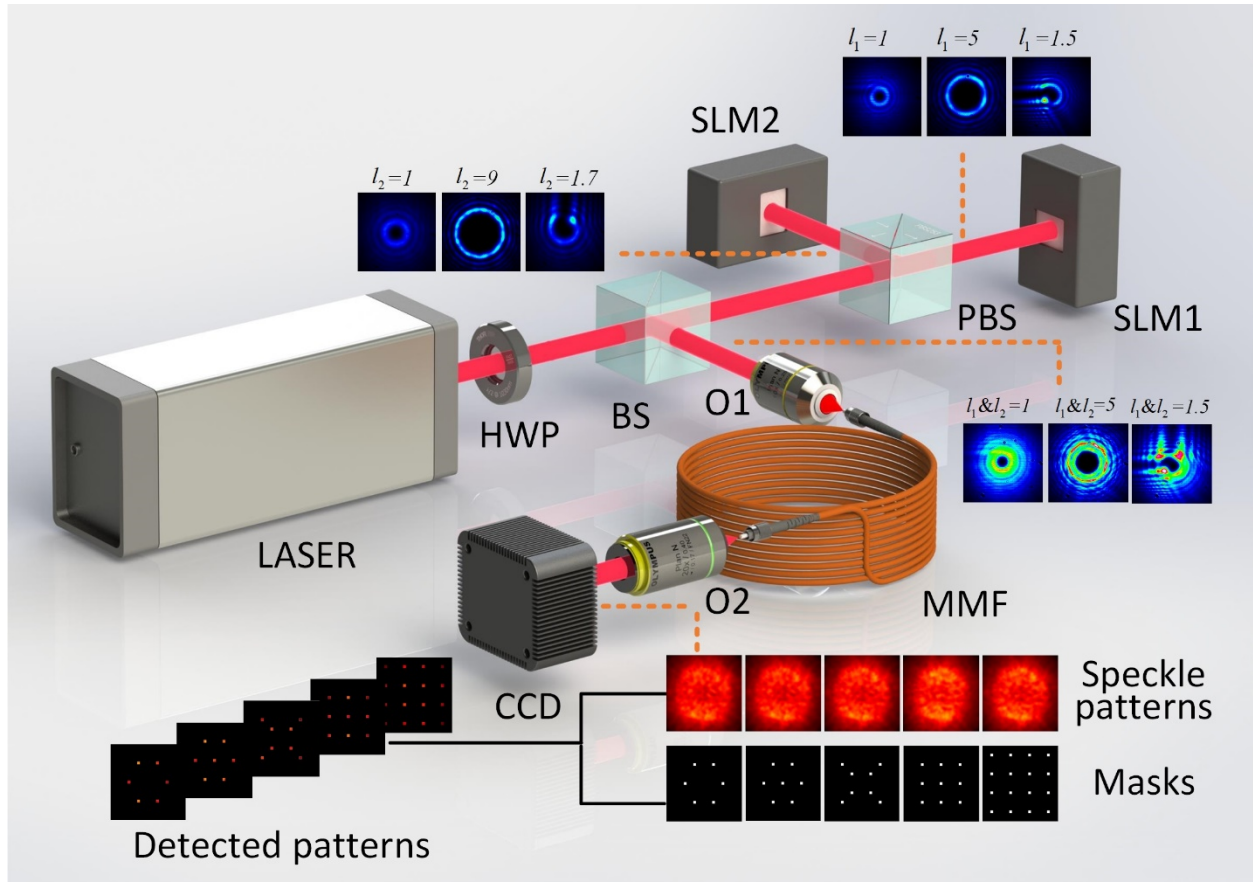


Fig. 2 Experimental setup. Two orthogonally polarized vortex beams are coupled into an MMF, generating speckle patterns at the distal end of the MMF, which are captured by a spatially masked CCD camera that functions as an array of single-pixel detectors. Abbreviations: BS, beam splitter; CCD, charge-coupled device; HWP, half-wave plate; MMF: multimode fiber; O1 and O2, microscope objective; PBS, polarizing beam splitter; SLM1 and SLM2, spatial light modulator.

On the SLM, the OAM of spiral phases varies from 1 to 10.9 with an interval of 0.1, generating 100 phase variations. At each phase value, 10,000 different intensity-value sequences of the speckle field are recorded when the two OAMs change alternately. Upon imposing different masks on the speckle patterns, a simulated several SPDs strategy is realized. Finally, these intensity sequences of corresponding detectors are used as the input of the designed neural network.

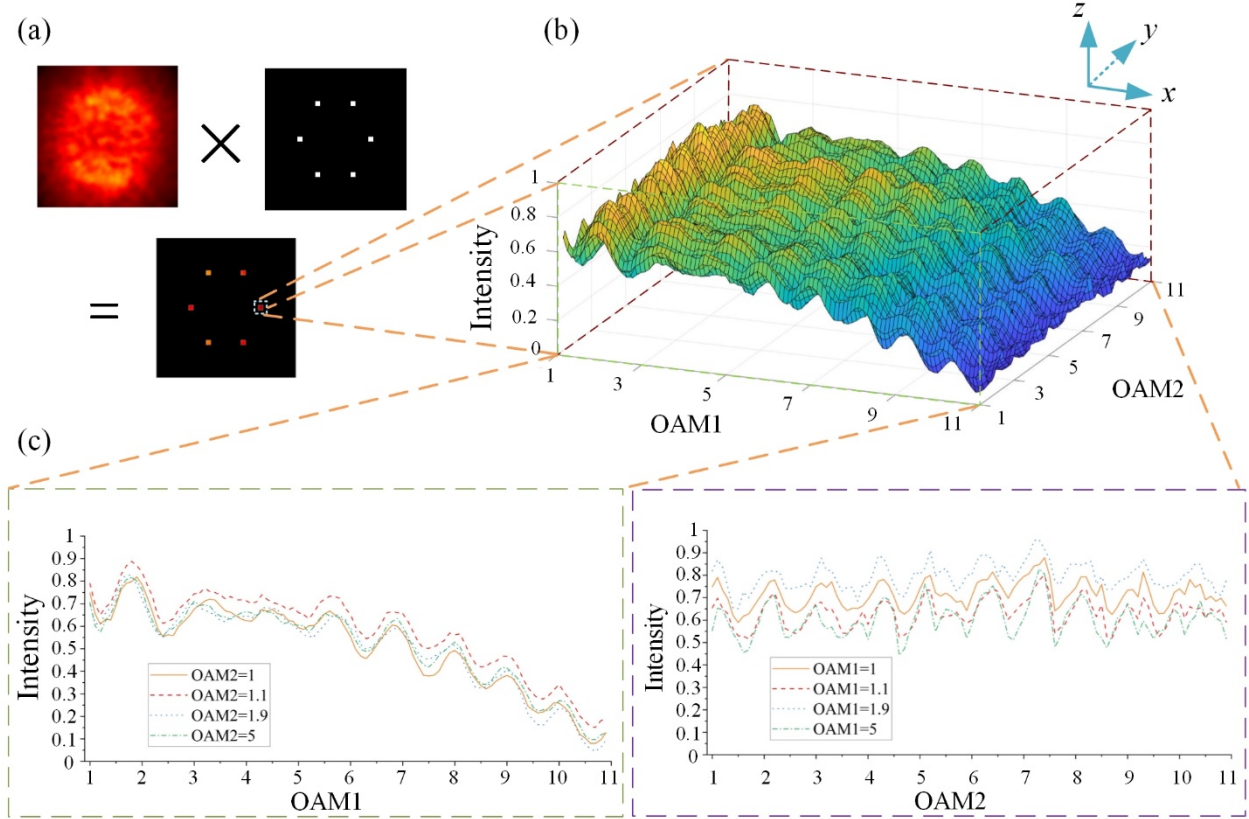


Fig. 3 Evolution of the intensity values of the OAM1 and OAM2 at one sampled position in the speckle field. (a) Exemplified speckle pattern from the MMF, 6-point mask (simulating an array containing 6 SPDs), and the sampled intensity distribution that is detected in experiment, whose intensity sequence will be used as the network input. (b) One example of intensity values at a SPD region in the speckle field generated by two orthogonally polarized vortex beams with different OAMs. (c) The evolution profiles of intensity values from the perspectives of OAM1 and OAM2, respectively.

Fig. 3 illustrates the evolution profiles of light intensity at one sampled SPD region in the speckle field. As shown in (a), the speckle field is imposed with a mask containing 6 points, resulting in the sampled light intensity distribution that is recorded in experiment. Fig. 3b displays the corresponding intensity values at the rightmost position of the speckle light field in (a) when two orthogonally polarized vortex beams of different OAM1 and OAM2 transmit through the MMF, which exhibits fluctuations with changes in OAMs (OAM1=1-10.9, and OAM2=1-10.9). To better visualize the trend, the evolution profiles are extracted in Fig. 3c from the perspectives

of OAM1 and OAM2, respectively. The periodic variations observed in Fig. 3c indicate that the MMF transmission system is ill-posed, making it very challenging to resolve different OAMs using only one point of light intensity information. However, this observation also provides insight into a potential solution to the ill-posed problem by increasing the number of SPDs. Notably, such a strategy exhibits clear contrast to former explorations on OAM recognition that mostly rely on the use of high-resolution cameras to capture the full field of view of the output patterns from the MMF.

3 Results

To study the influence of the area and the number of individual SPDs on the recognition accuracy, a CCD camera imposed with different masks is used in this study to simulate different arrays of SPDs. Areas of individual SPDs are quantified by a unit of ‘px’ that corresponds to the area of one single light-sensitive element ($7.4^2 \mu\text{m}^2$) in the CCD camera. For example, an SPD area of 5^2 px means 5 by 5 neighboring CCD elements are combined to form one SPD, while 9 points means there are 9 such SPDs on the CCD as imposed by the mask. For each individual SPD, the light intensities detected CCD light-sensitive elements are accumulated, and the recorded intensity sequence of the SPD array is used as the input for the network.

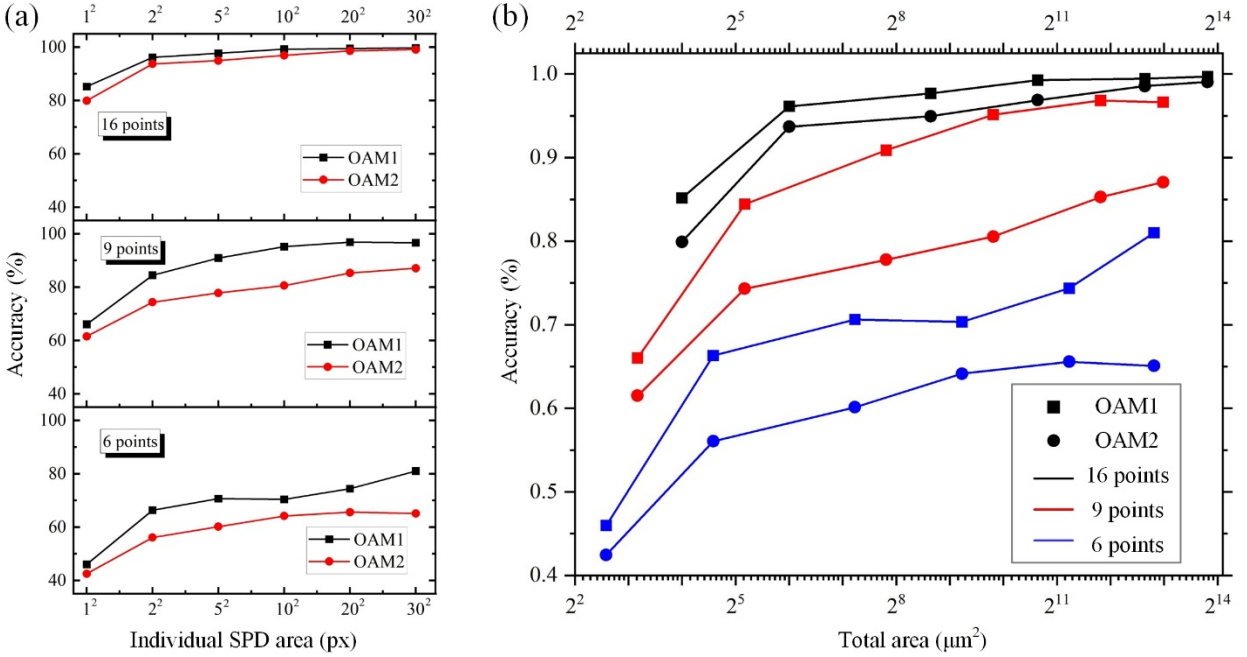



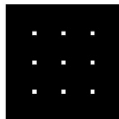

Fig. 4 The accuracy of predicting the OAMs of two orthogonally polarized vortex beams versus detector area with different number of SPDs from the perspective of (a) individual SPD area and (b) the total effective detecting area. The square sign and the circle sign represent for OAM1 and OAM2 respectively. .

As shown in Fig. 4a, a number of sets with different numbers and areas of SPDs were collected. They were not involved in the training process, and they were imported to test the performance of ROAM-ANN after the training process was completed. The results are shown in Fig. 4a (more detailed results in *Supplementary Note 1*). As seen, the recognition accuracies of the OAMs exceed 99% when the number of SPD equaled to 16 and each individual SPD area reached as largely as 30×30 px, demonstrating the applicability of SMPD with the aid of deep learning. The accuracies can still be higher than 93% even if the area of individual SPD is reduced to 2×2 px with 16 SPDs. That said, the trend is very clear that the recognition accuracy declines gradually with reduced number or area of SPDs. For example, with 6 SPDs of area of 1×1 px, the accuracies for OAM1 and OAM2 are both below 50%. To better visualize the trend, in Fig. 4b, the recognition accuracies are plotted as a function of the net area of SPDs for each set of measurements. As seen, we

calculated the total detecting area of each array, and the recognition accuracies using arrays with varying numbers of SPDs were compared. In comparison to the influence of effective detection area on recognition accuracy, results indicate that the number of SPDs has a more fundamental impact on recognition performance. Consequently, in practical implementations, there is a trade-off between the detecting area allocated to individual SPDs, which directly affects device size and cost, and the number of SPDs employed, which directly impacts the acquisition rate.

Next, we study how spatial deployment of the SPDs (sampling arrangement of the speckle field) affects the performance of OAM recognition. As shown in Table 1, the difference of recognition accuracy is negligible regardless of the variations of the deployment pattern, as long as the area and the number of the SPDs remain the same. Therefore, designating fixed positions between the source and the detector(s), as required in regular ballistic optical imaging and CGI³, does not constitute a prerequisite in our method to perform faithful OAM information interpretation, which forms a unique advantage over previous imaging strategies.

Table 1 Recognition results with different spatial deployments of SPDs (same area, same number)

Spatial allocations of 9 SPDs						
Recognition	OAM1	OAM2	OAM1	OAM2	OAM1	OAM2
accuracy (%)	89.40	78.05	95.15	80.55	93.85	79.70

To further demonstrate the potential of the proposed method in MMF-based communication, an optical data transmission system based on OAM-multiplexing was implemented experimentally. The scheme of the data transmission system is illustrated in Fig. 5. Two spiral phase images with a resolution of 100×100 px were encoded using 8-bit color depth. OAM bases of 2.1-2.8 were chosen for complex multiplexing (see *Supplementary Note 2* for details) to represent each pixel of

the encoded images. A digital micro-mirror device (DMD) was employed to effectively generate the multiplexed vortex beams, which contained the encoded data and were coupled into the MMF. After being transmitted through the MMF, speckle patterns were generated at the distal end of the MMF. Three groups of sampling masks of different numbers of sampling points (16, 9, and 4 points) were applied to the speckle pattern. For each group, two different individual SPD areas were adopted: one was 10×10 px (accumulating the intensity values from all CCD pixels in the designated area) and the other was 1×1 px. Finally, based on the trained neural network (please refer to *Supplementary Note 1* for details), the encoded 8-bit information were decoded. Figure 5 (c) illustrates two reconstructed images and the corresponding decoding performances. As shown, under the condition of 16 sampling points with individual SPD area of 10×10 px, the decoding error rates for the two images are both lower than 0.2%. If the size of individual SPD is reduced to 1×1 px, the error rates of the two reconstructed images increased slightly due to the ultra-small sensing region ($7.4^2 \mu\text{m}^2$) at each detection point. Notably, when the number of SPD is decreased to 4, the proposed neural network can still achieve a decoding accuracy of over 74% with individual SPD area of 10×10 px.

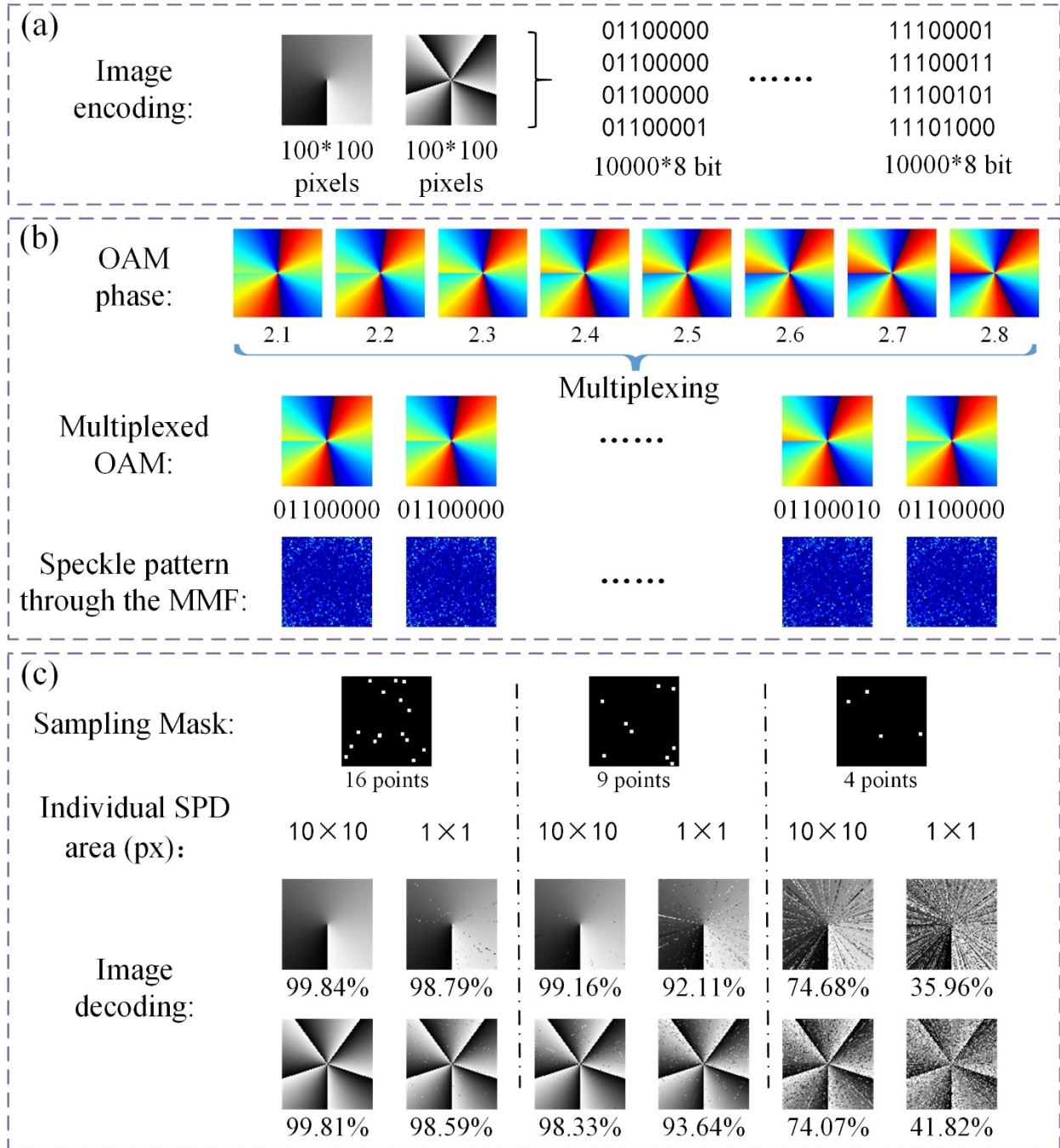


Fig. 5 The encoding and decoding procedures of the proposed method for retrieving images transmitted through MMF.

(a) Two spiral phase images are encoded accordingly by two 10000*8-bit rows. (b) The process of multiplexing using OAMs between 2.1-2.8, and the corresponding speckle pattern is generated after transmission through an MMF. (c) The distribution of the sampling SPDs on the output field and the decoded images shown with the corresponding accuracy.

4 Discussions

In regular imaging, it is challenging to resolve the full picture of an object if only a very small portion of the field of view of the object is captured or recorded by detector(s). The formation of speckle patterns due to mode dispersion through a multimode fiber offers unique characteristics of seemingly random and spatially redundant superposition of information¹⁹. Leveraging this feature, researchers can now reconstruct the input information using just a small portion of the speckle field³⁵. At present, methods such as collecting time sequential information using a single pixel detector or detecting spatial distribution information using a high-resolution detector are employed to collect the information in the output field. In this work, the proposed single-shot SMPD method is inspired by the fact that information projected onto one speckle grain on the output plane, in theory, is the superposition of the correspondence of the entire incident light field. In our method, one employs several small-area SPDs to collect spatial multiplexed intensity information on the speckle field. The method can significantly increase the detection speed but reduce the detection costs, and holds great promise for imaging and sensing infrared or ultraviolet wavebands, which still sees technological and economic challenges with wide-field sensors like CCD or CMOS cameras.

To demonstrate the feasibility of the proposed method, we applied it to the recognition of OAM, which has garnered significant attention in recent years^{36-41,44,45}. Heretofore, wide-field resolved cameras play an essential role in these OAM recognition applications to capture the intensity distribution at the output of the system, and high-resolution sampling for sensing is usually preferred. To the best of our knowledge, existing implementations typically require recorded output fields that are equal to or greater than 200×200 pixels^{38,39,41,43,44}. In contrast, this study hypothesizes that using a limited number of SPDs that spatially cover only a very small portion of

the speckle pattern might suffice for recognizing the OAMs of vortex beams. To validate this hypothesis, we developed a neural network referred as ROAM-ANN to examine SMPD with varying numbers and areas of SPDs. To achieve a decoding accuracy of over 98% as shown in Fig. 5, the net detector area and the corresponding spatial sampling rate in our method are $\sim 0.024\%$ of those adopted in a typical pattern-based configuration (i.e., $16 \times 1 \times 1$ px compared to 256×256 px)³⁸. Hence, with the proposed method, spatially resolved cameras are no longer necessary for recognizing OAM from speckle patterns. Instead, speckle intensity information from a minimal amount of SPDs is enough, opening venues for high throughput yet low-cost detection solutions to a wide range of field applications.

It should be clarified that in our exemplified experiments in this study, a CCD camera equipped with designated marks was employed to serve as an tunable array of SPDs. By this means, the influence of the number, area, and spatial distribution of the SPDs can be explored one by one. The results in Fig. 4 and Fig. 5 show that increasing the number of SPDs leads to improved recognition accuracy, which is natural as the neural network can learn more accurate features from more detailed and more comprehensive information. For the same reason, it can be observed that a larger area of SPD exhibits more robust results compared with a smaller one, as a larger area of detection reduces the impact of local anomalies as well as the influence of dark spots on the speckle field and hence exhibits stronger resistance to environmental noise. Moreover, the spatial allocation of the SPDs induce low impact to the recognition performance according to Table 1 and Fig. 5. The sampled detection locations can be sparsely allocated or merged into an integrated detection area as the first deployment pattern in Table 1. These results suggest that the recognition of OAMs with our method is robust and only minorly affected by the deployment pattern of the

sampled positions, which confers a higher degree of flexibility than that required in regular imaging systems.

Last but not the least, the experimental results have shown that the OAM information scrambled in the speckle field can be extracted by the proposed SMPD method using the neural network. Furthermore, our supplemental experiments demonstrate that the SMPD method could also be applied to other applications, such as recognizing the angle information of axicon (See *Supplementary Note 3*) and even to identifying the handwritten digits (See *Supplementary Note 4*). Such a capability can attribute to the transmission matrix theory of scattering medium, which suggests that the input object information is spread onto different regions of the resultant speckle field due to the accumulation of random multiple scattering²³. In theory, detection based on one SPD would be sufficient to extract the input information. However, since the transmission system is an ill-posed inverse problem, we do need a few numbers of SPDs in experiment to capture the in-situ intensity values for good performance. Therefore, it would be exciting if researchers can produce integrated SPD arrays to empower the proposed SMPD method as a practical high-efficiency, high-throughput, and cost-effective speckle-based imaging detection strategy.

5 Conclusion

In this work, we propose a method referred as SMPD that inquires the information carried by optical beams by recording the intensity values from several SPDs whose net sensing area constitutes only a very small portion ($<0.03\%$) of the full field of view of the speckle pattern. With the aid of the developed neural network, we successfully demonstrate that SMPD is capable of recognizing the OAMs of two orthogonally polarized vortex beams transmitting through MMF with high accuracies. The versatility of SMPD is further shown in its application to multiplexed-OAM decoding as well as handwritten digit recognition, with both scenarios yielding equally

promising results. Experiments further reveal that an increase in both the number and area of SPDs contributes positively to the accuracy of recognition tasks. Moreover, the position insensitivity of detectors in SMPD suggests promising flexibility of integration with various communication systems. In addition, the use of detectors without spatial resolution in SMPD extends the applied domain of techniques to a wider spectrum, compared with methods in which wide-field sensors are used. Future development of SMPD may enable high-fidelity, high-efficiency, high-throughput, and cost-effective imaging, sensing, and categorization of complex objects through scattering medium like multimode fibers.

Disclosures

The authors declare no conflicts of interest.

Acknowledgments

We thank Professor Tian Mo Shih at Xiamen University for his polish for the manuscript. This work was supported by the National Natural Science Foundation of China (Grant No. 62005086, 12150410318, 81930048), Key project of natural science foundation of Fujian Province (No. 2023J02020), Hong Kong Research Grant Council (15217721), Guangdong Science and Technology Commission (2019BT02X105), Shenzhen Science and Technology Innovation Commission (JCYJ20220818100202005), and Hong Kong Polytechnic University (P0038180, P0039517, P0043485, P0045762).

Code and Data Availability

The code and data underlying the results presented in this paper are not publicly available at this time but may be obtained from the authors upon reasonable request.

References

1. M. P. Edgar et al., "Principles and prospects for single-pixel imaging," *Nat. Photonics* **13**(1), 13-20 (2019).
2. C. F. Higham et al., "Deep learning for real-time single-pixel video," *Sci. Rep.* **8**(1), 2369 (2018).
3. R. V. Vinu et al. "Ghost diffraction holographic microscopy." *Optica* **7**(12), 1697-1704 (2020).
4. F. Wang et al., "Single-pixel imaging using physics enhanced deep learning," *Photonics Res.* **10**(1), 104-110 (2022).
5. H. Li et al., "Accelerating deep learning with high energy efficiency: from microchip to physical systems", *The Innovation* **3**(4), (2022).
6. Y. Zhou et al., "Low-consumption photoacoustic method to measure liquid viscosity," *Biomed. Opt. Express* **12**(11), 7139-7148 (2021).
7. H. Tao et al. "Artificial intelligence for medicine: Progress, challenges, and perspectives." *The Innovation Medicine* **1**(2), 100030-1(2023).
8. Z. Yu et al., "Wavefront shaping: A versatile tool to conquer multiple scattering in multidisciplinary fields," *The Innovation* **3**(5), (2022).
9. F. Wang et al., "Far-field super-resolution ghost imaging with a deep neural network constraint," *Light: Science & Applications* **11**(1), 1-11 (2022).
10. Z. Li et al., "Single-photon imaging over 200 km," *Optica* **8**(3), 344-349 (2021).
11. G. M. Gibson et al., "Single-pixel imaging 12 years on: a review," *Opt. Express* **28**(19), 28190-28208 (2020).
12. M. F. Duarte et al., "Single-pixel imaging via compressive sampling," *IEEE Signal Process Mag* **25**(2), 83-91 (2008).
13. M. Lyu et al., "Deep-learning-based ghost imaging," *Sci. Rep.* **7**(1), 1-6 (2017).
14. X. Mei et al., "Influence of the source's energy fluctuation on computational ghost imaging and effective correction approaches," *Chin. Opt. Lett.* **18**(4), 42602 (2020).

15. X. Lai et al., "Reconstructing images of two adjacent objects passing through scattering medium via deep learning," *Opt. Express* **29**(26), 43280-43291 (2021).
16. X. Zhang et al., "Different channels to transmit information in scattering media", *PhotoniX*. **4**(1), 1-13 (2023).
17. X. Zhang et al., "Physical origin and boundary of scalable imaging through scattering media: a deep learning-based exploration", *Photonics Res.* **11**(6), 1038-1046 (2023).
18. H. Li et al., "Towards ideal focusing of diffused light via optical wavefront shaping", *Adv. Photonics*. **5**(2), 20502 (2023).
19. H. Li et al., "Learning-based super-resolution interpolation for sub-Nyquist sampled laser speckles", *Photonics Res.* **11**(4), 631-642 (2023).
20. S. Cheng et al. "Alternating projection-based phase optimization for arbitrary glare suppression through multimode fiber." *Optics and Lasers in Engineering* **161**, 107368 (2023).
21. S. Cheng et al. "Long-distance pattern projection through an unfixed multimode fiber with natural evolution strategy-based wavefront shaping." *Opt. Express* **30**(18), 32565-32576 (2022).
22. W. Fan et al., "High - Fidelity Image Reconstruction through Multimode Fiber via Polarization - Enhanced Parametric Speckle Imaging," *Laser Photonics Rev.* **15**(5), 2000376 (2021).
23. S. M. Popoff et al., "Measuring the transmission matrix in optics: an approach to the study and control of light propagation in disordered media," *Phys. Rev. Lett.* **104**(10), 100601 (2010).
24. M. Lyu et al., "Learning-based lensless imaging through optically thick scattering media," *Adv. Photonics* **1**(3), 36002 (2019).
25. L. Allen et al., "Orbital angular momentum of light and the transformation of Laguerre-Gaussian laser modes," *Phys. Rev. A* **45**(11), 8185 (1992).
26. S. Fu et al., "Universal orbital angular momentum spectrum analyzer for beams," *PhotoniX* **1**(1), 1-12 (2020).

27. S. Fu et al., "Orbital angular momentum comb generation from azimuthal binary phases," *Adv. Photonics Nexus* **1**(1), 16003 (2022).
28. A. M. Yao et al., "Orbital angular momentum: origins, behavior and applications," *Adv. Opt. Photonics* **3**(2), 161-204 (2011).
29. Y. Shen et al., "Optical vortices 30 years on: OAM manipulation from topological charge to multiple singularities," *Light: Science & Applications* **8**(1), (2019).
30. Y. Chen et al., "Underwater transmission of high-dimensional twisted photons over 55 meters," *PhotoniX* **1**, 1-11 (2020).
31. Y. Yang et al., "Optical trapping with structured light: a review," *Adv. Photonics* **3**(3), 34001 (2021).
32. J. Chen et al., "Engineering photonic angular momentum with structured light: a review," *Adv. Photonics* **3**(6), 64001 (2021).
33. Z. Liu et al., "Non-line-of-sight optical communication based on orbital angular momentum," *Opt. Lett.* **46**(20), 5112-5115 (2021).
34. J. Wang et al., "Orbital angular momentum and beyond in free-space optical communications," *Nanophotonics* **11**(4), 645-680 (2022).
35. Lyu, Meng, et al., "Learning-based lensless imaging through optically thick scattering media." *Adv. Photonics* **1**(3), 036002 (2019).
36. F. Meng et al., "Measuring the magnetic topological spin structure of light using an anapole probe," *Light: Science & Applications* **11**(1), 1-9 (2022).
37. L. Chen et al., "Estimating topological charge of propagating vortex from single-shot non-imaged speckle," *Chin. Opt. Lett.* **19**(2), 22603 (2021).
38. Z. Wang et al., "Recognizing the orbital angular momentum (OAM) of vortex beams from speckle patterns," *Sci. China Phys. Mech. & Astron.* **65**(4), 244211 (2022).
39. F. Feng et al., "Deep learning-enabled orbital angular momentum-based information encryption transmission," *Acs Photonics* **9**(3), 820-829 (2022).

40. Q. Zhao et al., "Measuring high orbital angular momentum of vortex beams with an improved multipoint interferometer," *Photonics Res.* **8**(5), 745-749 (2020).
41. Y. Liu et al., "Learning-enabled recovering scattered data from twisted light transmitted through a long standard multimode fiber," *Appl Phys Lett* **120**(13), 131101 (2022).
42. J. Wang, "Twisted optical communications using orbital angular momentum," *Sci. China Phys. Mech. & Astron.* **62**(3), 1-21 (2019).
43. L. Gong et al., "Optical orbital-angular-momentum-multiplexed data transmission under high scattering," *Light: Science & Applications* **8**(1), 27 (2019).
44. Z. Liu et al., "Superhigh-resolution recognition of optical vortex modes assisted by a deep-learning method," *Phys. Rev. Lett.* **123**(18), 183902 (2019).
45. T. Giordani et al., "Machine learning-based classification of vector vortex beams," *Phys. Rev. Lett.* **124**(16), 160401 (2020).

Supplementary Material for: “Single-shot recognition of orbital angular momentum from speckles with spatially multiplexed point detection”

Zhiyuan Wang,^{a,b,†} Haoran Li,^{c,d,†} Qi Zhao,^{c,d} Vinu R V,^{a,b} Xiaocong Yuan,^e Ziyang Chen,^{a,b,*} Puxiang Lai,^{c,d,f,*} and Jixiong Pu^{a,b}

^aHuaqiao University, College of Information Science and Engineering, Xiamen, 361021, China

^bHuaqiao University, Fujian Provincial Key Laboratory of Light Propagation and Transformation, Xiamen, 361021, China

^cHong Kong Polytechnic University, Department of Biomedical Engineering, Hong Kong, China

^dHong Kong Polytechnic University, Shenzhen Research Institute, Shenzhen, China

^eShenzhen University, Nanophotonics Research Center, Shenzhen Key Laboratory of Micro-scale Optical Information Technology, Institute of Microscale Optoelectronics, Shenzhen, 518060, China

^fHong Kong Polytechnic University, Photonics Research Institute, Hong Kong, China

*Address all correspondence to Ziyang Chen at ziyang@hqu.edu.cn and Puxiang Lai at puxiang.lai@polyu.edu.hk

[†]These authors contributed equally to this work.

Supplementary Note 1: Network structure and the training process

A dual-path neural network is designed to extract the spatial association features in the light intensity sequence and the correlation among its elements, respectively, as illustrated in Fig. S1. The input sequence is fed into two paths: one is a convolution path, and the other is a fully connected path. In the convolution path, the sequence is processed by multiple one-dimensional convolution layers that stack spatially correlated high-dimensional features at the feature channels. The other path, namely the fully connected path, shoulders the responsibility for extracting the distributed characteristics of the original sequence. The high-dimensional features from the convolution path flow into a GlobalAveragePooling1D layer and then concatenate with the tensor from the fully connected path to form a feature tensor. Finally, the blended feature tensor is passed through the output modules and the output is generated by applying the *softmax* function to the separate tensors.

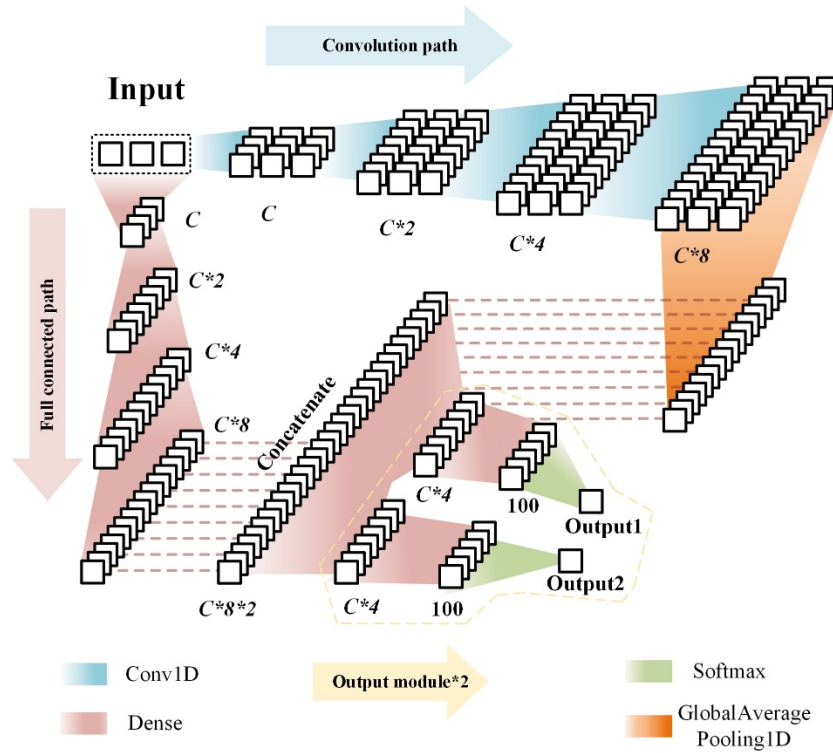


Fig. S1 Structure of the ROAM-ANN. Conv1D, one-dimensional convolution layer; GlobalAveragePooling1D, global average pooling operation for temporal data. The number of channels (C) and output modules can be adjusted according to the object to be recognized.

One-hot encoding, which uses N -bit binary values to represent N categories that are mutually exclusive, is employed to encode the OAMs. To prevent the intensity-value sequence from being reduced during the convolution path, the padding value of the convolution layers is set to the “same”. This allows the network to handle the intensity-value sequences of varying lengths that are generated by different numbers of SPDs. The network is implemented based on Tensorflow 2.6, and the training and testing processes are carried out on a server equipped with a GPU (NVIDIA P620) for all groups. The dataset is randomly split into training and testing sets at an 8:2 ratio. The network is trained for different epochs based on the recognition object, using Adam¹ as the optimizer. The detailed training parameters are listed in Table S1. The initial learning rate of Adam, for different tasks, has a specific decay strategy as listed in Table S1. The binary cross-

entropy loss function is chosen, and the network's performance is evaluated based on the accuracy of recognition defined by

$$Accuracy = \frac{\sum_{i=1}^n equal(\arg \max(y_{pred}^i), \arg \max(y_{true}^i))}{n}, \quad (1)$$

where y_{pred}^i and y_{true}^i denote the predictions from the network and encoded-OAMs, respectively; function $Argmax(\cdot)$ returns the position where the maximum value is located; function $equal(\cdot)$ determines whether two values are equal, and a Boolean value of 0 or 1 is returned, representing unequal or equal, respectively. Lastly, parameter n represents the total number of network predictions.

Table S1 Training paraments for recognition tasks in the manuscript

Recognition object	OAMs	Multiplexed-OAMs	Angle of axicons	Hand-written digits
C	16	32	16	16
Training epochs	120	50	120	120
Batch size	16	256	32	32
Initial learning rate	1e-3	2e-4	1e-3	1e-3
Decay rate	0.1	0.6	0.1	0.1
Decay epoch	60 th & 100 th	Every 5 epochs	60 th & 100 th	60 th & 100 th
Output modules	2	1	1	1
Output units	100	256	100	10

Table S2 Detailed recognition accuracies of the OAMs with different numbers and areas of SPDs

Number of SPDs	Areas (px)	1 ²	2 ²	5 ²	10 ²	20 ²	30 ²
	OAMs	Accuracy (%)					
16	OAM1	85.17	96.13	97.67	99.26	99.45	99.70
	OAM2	79.91	93.70	94.94	96.88	98.56	99.06
9	OAM1	66.02	84.42	90.87	95.14	96.83	96.63
	OAM2	61.51	74.31	77.78	80.56	85.27	87.05
8	OAM1	61.76	81.60	85.57	87.25	90.53	90.97
	OAM2	52.03	69.74	70.78	68.20	72.32	75.94
7	OAM1	56.50	76.59	82.59	83.78	85.66	87.35
	OAM2	55.65	70.44	74.80	69.79	70.98	73.36

6	OAM1	45.98	66.32	70.63	70.34	74.36	81.00
	OAM2	42.46	56.05	60.12	64.14	65.58	65.08

Table S2 shows the detailed recognition results of Fig. 4 in the manuscript. The evolution of losses and accuracies of ROAM-ANN for decoding multiplexed OAMs during the training process are shown in Fig. S2.

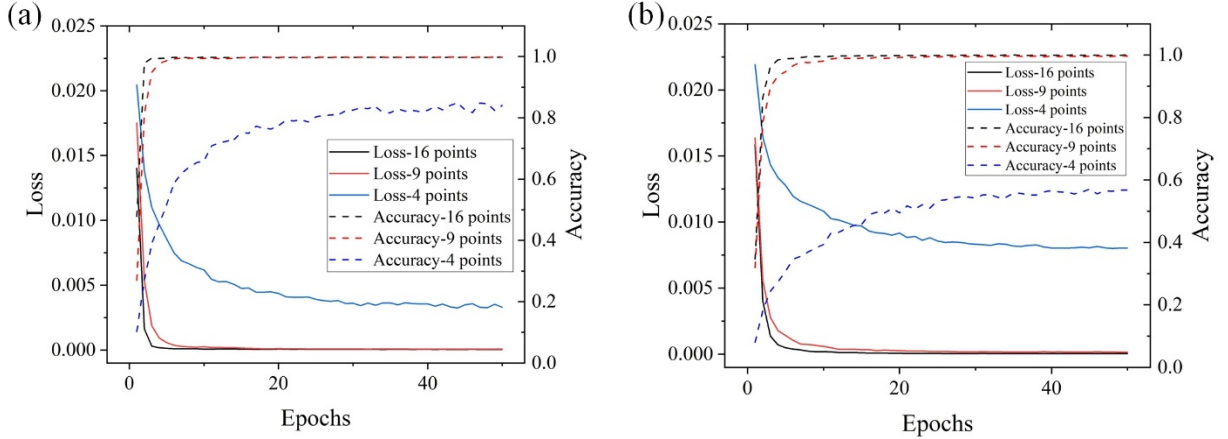


Fig. S2 The evolution of loss and accuracy of ROAM-ANN for decoding multiplexed OAMs during the training process with individual SPD area of 10×10 px (a) and 1×1 px (b), respectively.

Supplementary Note 2: OAM multiplexing and complex modulation by DMD

During the encoding process of OAM multiplexing, an 8-bit binary grayscale value is encoded by the superposition of 8 OAM beams with topological charges 2.1-2.8. “1” and “0” in the 8-bit value indicate whether the OAM beam at the corresponding position participates in the superimposition. To avoid different encoding grayscale values corresponding to the same light field of OAM multiplexing, complex amplitude superposition of OAM beams instead of phase superposition is adopted in this work. Besides, for simplifying the complexity of the superposition, we change the complex amplitude expressions of fractional-order OAM beams to the expressions of integer-order OAM beams, which is

$$OAM_m(r, \theta) = \frac{1}{\omega_0} \left(\sqrt{2} \frac{r}{\omega_0}\right)^m \exp\left(-\frac{r^2}{\omega_0}\right) \exp(im\theta), \quad (2)$$

where m is the topological charge, θ denotes the azimuthal angle, and ω_0 is the beam waist radius. According to this expression, the amplitude distribution of fractional-order OAM beams is the same as the integer-order OAM beams with a complete circular distribution. The process of encoding gray values through OAM multiplexing is shown in Fig. S3.

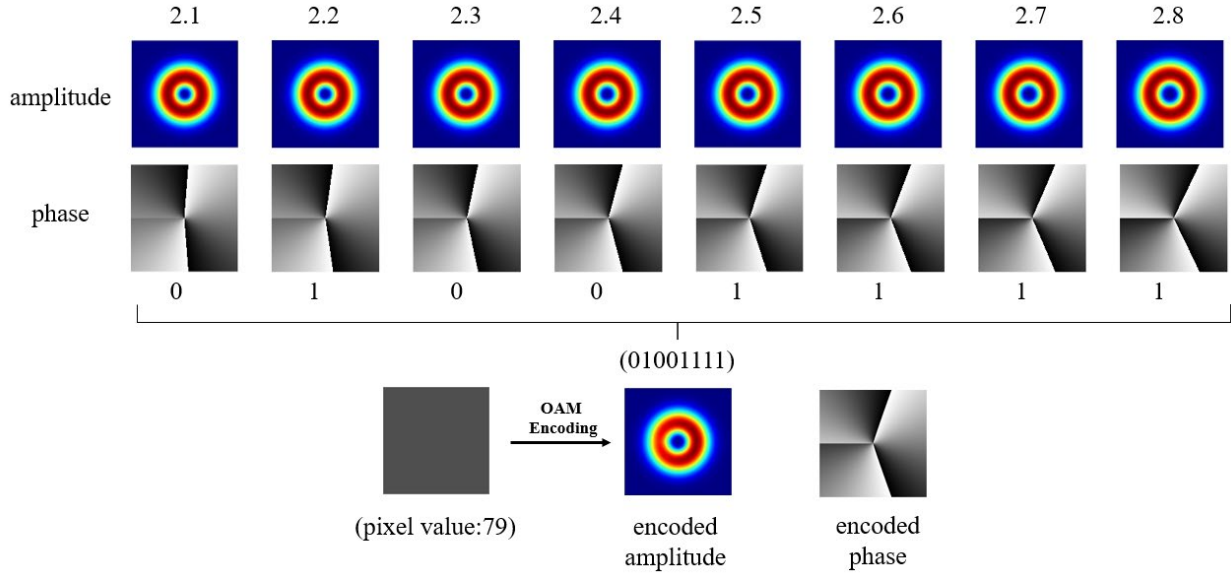


Fig. S3 The scheme of encoding 8-bit binary grayscale value with OAM beams of 2.1-2.8

Since the complex amplitude light field superimposed by the different OAM beams needs to be realized at the proximal end of the multimode fiber (MMF) as the input to obtain the corresponding speckle light field, it's crucial to use a digital mirror device (DMD, DLP7000 Texas Instruments Inc, USA) which can only achieve binary modulation as a complex amplitude modulation device. For this purpose, we use an optimized Lee hologram method combined with a 4f spatial filtering system to achieve high-quality complex amplitude modulation^{2,3}. First, the complex amplitude is encoded into the corresponding binary computer-generated hologram (CGH) based on the following formula²:

$$t(x, y) = A \cos(2\pi(x - y)\beta - \varphi(x, y)),$$

$$h(x, y) = \begin{cases} 1, & t(x, y) \geq 0 \\ 0, & t(x, y) < 0 \end{cases}, \quad (3)$$

where A represents the normalized amplitude, $\varphi(x, y)$ denotes the phase, β is the designed carrier frequency, and $h(x, y)$ is the calculated CGH by the Lee method. Then, an error diffusion method is used to further optimize the CGH obtained in the previous step, so that it can achieve the goal of more precise complex amplitude modulation³. Since the final obtained CGH is the hologram formed by the interference of the complex amplitude light field of the target and the reference light with a specific carrier frequency, after passing through the first lens of the $4f$ system, three distinctly different diffraction orders (-1, 0, +1) will be generated on the Fourier plane. By using a spatial filter to select the -1 order, the corresponding complex amplitude modulation of the target is achieved after passing the second lens of the $4f$ system. Fig. S4 and Fig. S5 respectively show the method of using a DMD to achieve complex amplitude modulation and the experimental setup for realizing OAM multiplexing.

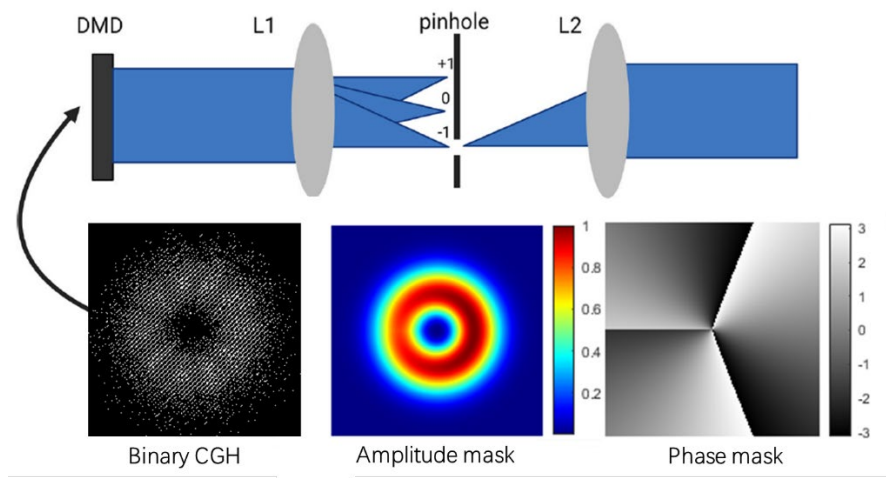


Fig. S4 The scheme for achieving complex amplitude modulation by a DMD

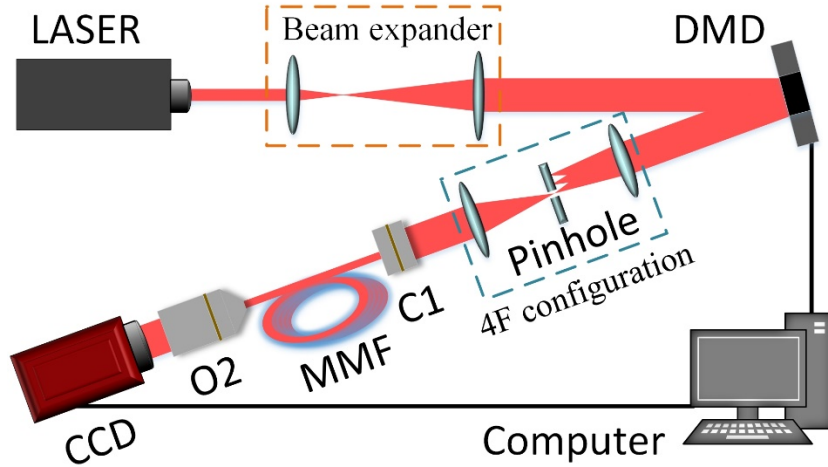


Fig. S5 Experimental setup for realizing OAM multiplexing

The light beam emitted from a 532 nm continuous-wave laser (EXLSR-532-300-CDRH, Spectra Physics, USA) undergoes expansion using a beam expander. The expanded beam is directed towards a digital mirror device (DMD, DLP7000, Texas Instruments Inc) where the beam reflected and modulated before being relayed into a 4f system. The modulated beam is then coupled into an MMF (0.22 NA, 200 μm core diameter, SUH200, Xinrui, China) via a collimator. The output field from the MMF is condensed via an objective (O2, 20X, NA=0.4, Olympus) and finally collected by a CCD camera. Based on the above system, the DMD loads the CGHs corresponding to gray pixel values ranging from 0 to 255, which is repeated 10 times. Subsequently, three spiral phase images, each with dimensions of 100×100 pixels, were encoded into 30,000 CGHs, which are then loaded onto the DMD. To mitigate the impact of environmental noise, the CGHs associated with gray pixel values from 0 to 255 are once again captured in 10 repetitions after the transmission of the images. In summary, the training dataset consists of 5,120 intensity-label pairs, and the testing set comprises 20,000 CGHs corresponding to the transmitted images.

Supplementary Note 3: Recognizing the angle of axicons

Long-distance focused Bessel beams can be generated using an axicon. Axicons with different angles yield unique phase structures, enabling flexible controls of the beam's focal position according to the angle of the axicon. Thus, determining the axicon angle is essential for generating a specific long-distance focused beam. However, when light that carries the phase information of an axicon transmits through a multimode fiber, the information becomes disrupted. It remains unsettled for existing methods to extract the angle information of the axicon from speckles.

To further demonstrate the effectiveness of SMPD, we designed a simulation to measure the angle of axicons of Bessel beams. Similar to the one described in the main text, we sampled several regions from the speckle field for intensity recording via the masked CCD camera. These intensity values were then used for network training and testing, and the neural network eventually output the extracted axicon angle information from the speckle field. Fig. S6 illustrates the generation of corresponding speckle patterns when light carrying various angle information of axicons passes through a scattering medium. In the simulation, the angle of the axicon varies from 0.1 to 10 degrees with an interval of 0.1. Note that a small portion of the axicon phase were deliberately removed in experiment. By rotating each axicon phase 50 times, we can obtain a more diverse dataset and improve the network's robustness. In the speckle field, 16 sample points of size 30×30 px were selected to measure and record the intensity value. Like in the main text, the experiment obtained 5,000 sets of intensity sequence, which was input into the network for training. The parameters of the neural network and the training process are listed in Table S1.

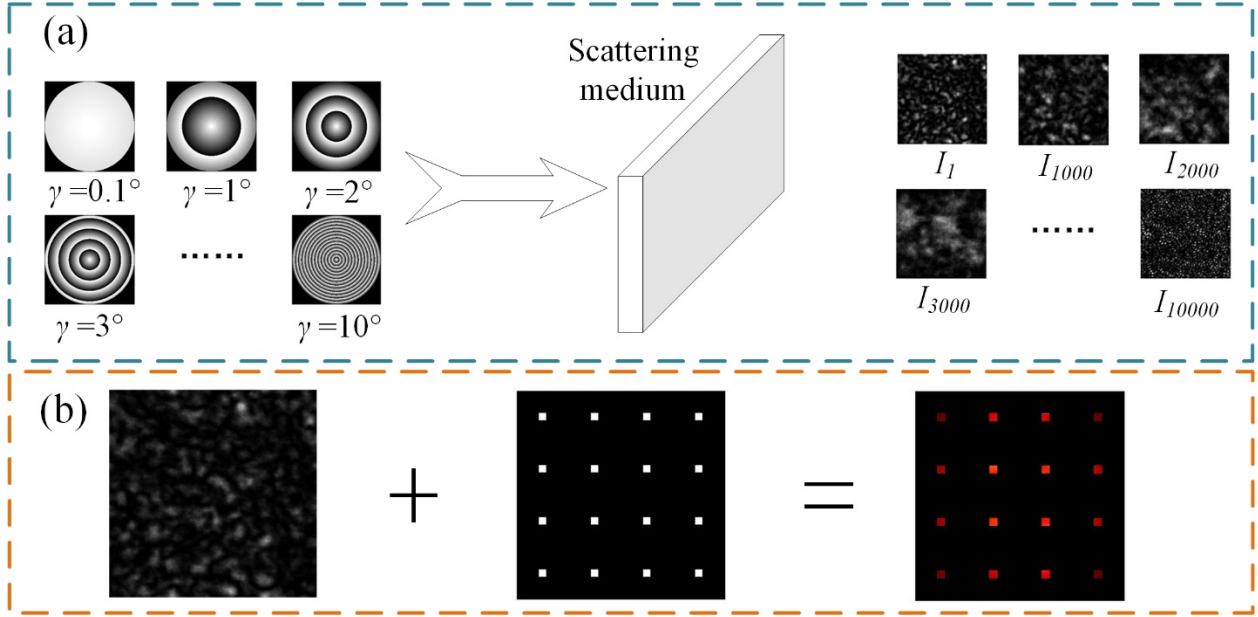


Fig. S6 (a) Bessel beams with different angles of axicon phases transmit through a scattering medium, forming speckle patterns. (b) Illustration of sampled detection of the speckle field with 4×4 SPDs.

Fig. S7 shows the evolution of the loss and accuracy during the network training process. By optimizing the learning rate, both loss function and recognition accuracy could be substantially improved. After 120 epochs, the network could achieve an accuracy of 88% on the validation set (Note: the validation set participates in the training process and is used to determine hyperparameters in the network model). Finally, it achieved an accuracy of 88.25% on the testing set, which was not involved in the training process.

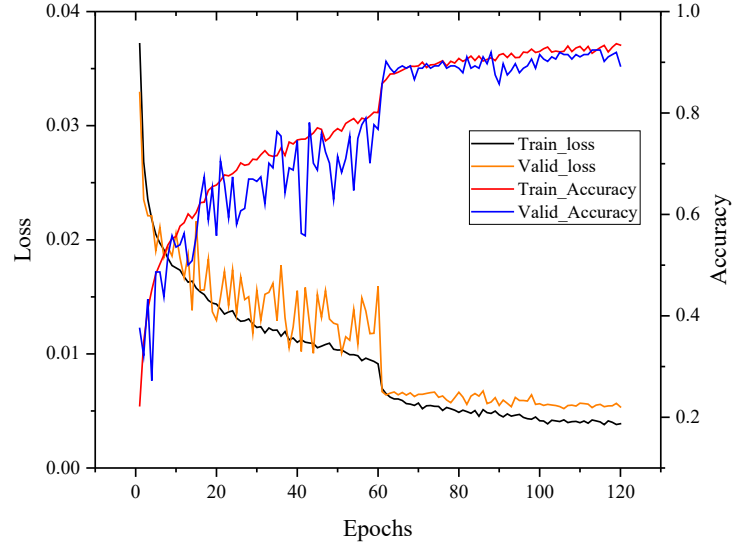


Fig. S7 The evolution curves of the loss and accuracy during the training process for recognizing the angle of axicons

Supplementary Note 4: Recognizing hand-written digits

Current practice of recognizing handwritten digits from speckles typically involves feeding complete speckle images to extract the spatial distribution features of the encoded information and accomplish the objective of digit classification. With the proposed SMPD method, as illustrated in Fig. S8, 16 SPDs were selected to record intensity values as the network input. Simulation was conducted using hand-written digit images from the MNIST dataset; the intensity information of the images was scrambled into speckle patterns and was recorded by the 16 SPDs that were randomly distributed in space with an area 10×10 px for each individual SPD. These intensity values, together with their corresponding Ground Truth labels, constituted 60,000 intensity-label pairs. Among these pairs, 40,000 were selected for neural network training, 10,000 for network validation, and the remaining 10,000 for testing the network performance. The variations in loss and accuracy during the network training process are given in Fig S8, and the parameters of the neural network and the training process are listed in Table S1. Finally, the network achieved a recognition accuracy of $\sim 74\%$ on the testing dataset.

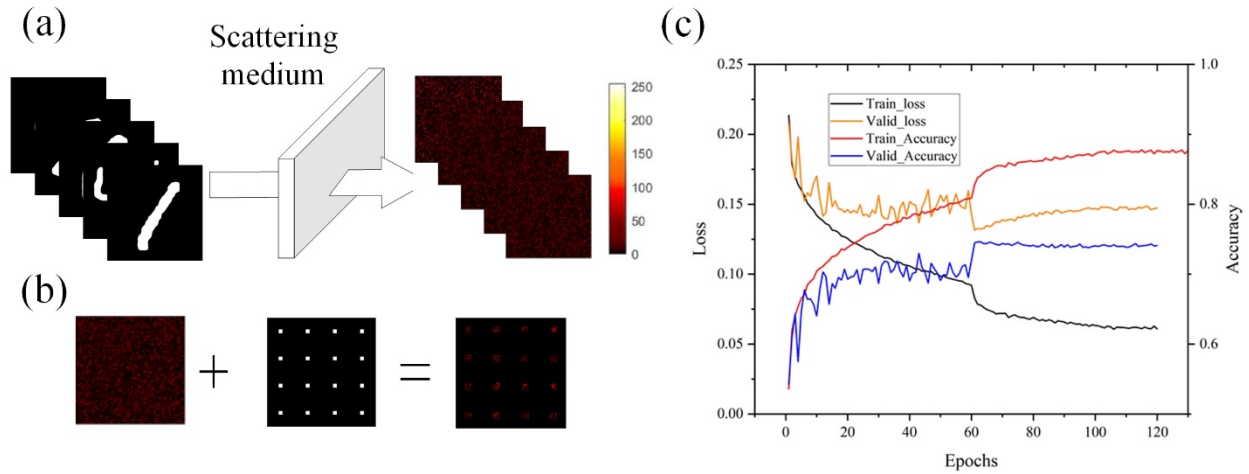


Fig. S8 (a) Hand-written digits transmit through a scattering medium, forming speckle patterns. (b) Illustration of sampled detection of the speckle field with 4×4 SPDs. (c) The evolution curves of the loss and accuracy during the training process for recognizing the hand-written digits.

References

1. D. P. Kingma et al., "Adam: A method for stochastic optimization," *arXiv preprint arXiv:1412.6980* (2014).
2. Lee, Wai-Hon. "Binary computer-generated holograms." *Applied Optics* 18.21 (1979): 3661-3669.
3. Hu, Xinyao, et al. "Dynamic shaping of orbital-angular-momentum beams for information encoding." *Optics express* 26.2 (2018): 1796-1808.